

RESEARCH ARTICLE | MAY 01 2023

Signal-processing electronics for stable and sensitive weak-field atomic vector magnetometers

H. Zhou; X.-K. Wang; S.-Q. Liu; ... et. al



Rev Sci Instrum 94, 054701 (2023)

<https://doi.org/10.1063/5.0150256>



CrossMark

Articles You May Be Interested In

Domain of generalized Riesz difference operator of fractional order in Maddox's space $\ell(p)$

AIP Conference Proceedings (February 2021)

Impact ionization model for full band Monte Carlo simulation

Journal of Applied Physics (April 1994)

Raman and nuclear magnetic resonance investigation of alkali metal vapor interaction with alkene-based anti-relaxation coating

J. Chem. Phys. (March 2016)

Time to get excited.
Lock-in Amplifiers – from DC to 8.5 GHz

Find out more

Signal-processing electronics for stable and sensitive weak-field atomic vector magnetometers

Cite as: Rev. Sci. Instrum. 94, 054701 (2023); doi: 10.1063/5.0150256

Submitted: 13 March 2023 • Accepted: 15 April 2023 •

Published Online: 1 May 2023



View Online



Export Citation



CrossMark

H. Zhou,¹ X.-K. Wang,¹ S.-Q. Liu,¹ L. Cheng,^{2,3} K. Liu,^{2,3} Z.-H. Pan,^{2,3} Y.-R. Li,^{2,3,4} X.-J. Hao,^{2,3,a)} D. Sheng,^{1,4,a)} and Y.-M. Wang^{2,3}

AFFILIATIONS

¹Department of Precision Machinery and Precision Instrumentation, Key Laboratory of Precision Scientific Instrumentation of Anhui Higher Education Institutes, University of Science and Technology of China, Hefei 230027, China

²School of Earth and Space Sciences, and Deep Space Exploration Laboratory, University of Science and Technology of China, Hefei 230026, China

³CAS Center for Excellence in Comparative Planetology, and CAS Key Laboratory of Geospace Environment, Hefei 230026, China

⁴Hefei National Laboratory, University of Science and Technology of China, Hefei 230088, China

^{a)}Authors to whom correspondence should be addressed: xjhao@ustc.edu.cn and dsheng@ustc.edu.cn

ABSTRACT

We present the electronics developed for a sensitive and stable atomic vector magnetometer used in low-field detections. These electronics are required to be not only highly reliable and sophisticated for signal processing but also compact in size and low cost in resource consumption for the purpose of miniaturization. In addition, this magnetometer works with multiple modulations, where the interferences between harmonics of modulation fields often disturb the long-term measurements of the sensor. We work out a robust method to eliminate this problem by choosing the modulation frequencies with separations to match the minimum response points of the low-pass filters used in the demodulation processes. We validate the performance of the electronics and the frequency-selection scheme of the modulation fields with corresponding experimental results.

Published under an exclusive license by AIP Publishing. <https://doi.org/10.1063/5.0150256>

I. INTRODUCTION

Due to high sensitivities and stabilities, optically pumped atomic magnetometers have wide applications in fields, such as fundamental physics research,^{1,2} bio-imaging,^{3,4} geophysics surveys,⁵ and space science.⁶ Recently, we have developed a compact three-axis atomic magnetometer for weak field detections.⁷ With the help of Herriott cavities inside the atomic cell, this Rb magnetometer works in a relatively low temperature (75 °C), which is favorable for measurement stability. This sensor has been demonstrated to reach a noise level better than 45 fT/Hz^{1/2} at 1 Hz and measurement stability better than 1.5 pT at an integration time of 10⁴ s for all three axes, even with the laser frequency free running. This level of stability is comparable with the state-of-art scalar magnetometers,⁸ and this sensor provides an important step toward ultra-low field calibration.

In previous demonstrations, the signal-processing electronics for the aforementioned sensor are mostly commercial products. For purposes of miniaturization and mobility, we need to develop compact and high precision electronics to match the high performance of the sensor. These home-made electronics can be applied to similar atomic sensors that require signal demodulations and closed-loop operations. In addition, since multiple modulation fields with different frequencies are present when the sensor is working, the signals in feedback loops have additional components from the interference between harmonics of modulation fields, among which the low frequency components have been identified to disturb the long-term stability of the sensor. We have to carefully choose the modulation frequencies in previous tests to get around this problem. This has been a common problem for atomic magnetometers with multiple modulation fields, and we take the opportunity of building the signal-processing electronics to work out a robust solution.

In this paper, we demonstrate the signal-processing electronics designed for the highly sensitive and stable three-axis atomic magnetometer and present a practical scheme to eliminate the interference problem from the multiple modulation fields. Following this introduction, Sec. II describes the working principle of the sensor, Sec. III covers electronics design, Sec. IV presents the experimental results on the performance of the developed electronics and the scheme to solve the signal-interference problem, and Sec. V describes the work following the development in this paper.

II. WORKING PRINCIPLE OF THE ATOMIC MAGNETOMETER

The previously developed atomic magnetometer operates with a zero-field level-crossing resonance scheme, and modulation fields with frequencies of kHz and amplitude of 100 nT are applied to the field coils.⁷ The atomic polarization \mathbf{P} is described by the Bloch equation,⁹

$$\frac{d\mathbf{P}}{dt} = \frac{1}{Q(P)} [\gamma_e \mathbf{P} \times \mathbf{B} - R_{op}(\mathbf{s} - \mathbf{P}) - R_{rel}\mathbf{P}], \quad (1)$$

where γ_e is the electron gyromagnetic ratio, \mathbf{B} is the external field, $Q(P)$ is the nuclear-spin slowing-down factor,⁹ R_{op} is the optical pumping rate, \mathbf{s} is the photon spin of the pump beam, and R_{rel} is the atomic depolarization rate in the absence of the laser beam. Suppose that the laser beam is along the z direction while the modulation field $B_m \cos \omega_m t$ is applied to the x direction, the component of the polarization along the laser beam direction modulated at ω_m is

$$P_z(\omega_m) = \frac{\gamma_e B_{x,0} R_{op} \sin(\omega_m t)}{R_{tot}^2 + (\gamma_e B_{x,0})^2} J_0 \left(\frac{\gamma_e B_m}{Q(P)\omega_m} \right) J_1 \left(\frac{\gamma_e B_m}{Q(P)\omega_m} \right), \quad (2)$$

where $B_{x,0}$ is the bias field along the x direction, $R_{tot} = R_{op} + R_{rel}$, and J_0 (J_1) is the zero-order (first-order) Bessel function of the first kind. The transmitted beam intensity can be expressed as $I_O = \sum_n a_n \sin(n\omega_m t + \phi_n)$ with a_1 proportional to $B_{x,0}$. By demodulating the transmitted beam signal at the reference frequency of ω_m , we can extract the bias field along the x direction.

For a full three-axis field detection, the magnetometer contains a cell with double orthogonal multipass cavities, each with a circularly polarized pump beam injected in it (see Fig. 1). In addition, modulation fields with different frequencies are applied along three axes. Due to the non-orthogonality of the field coils and the non-parallel propagation of the beam between the cavity mirrors, the transmitted beam signal not only contains the harmonics of each modulation frequency but also complicated beating results between them. One possible consequence is that the beating signals of the low harmonics of the modulation fields survive the demodulation process and are fed back to the field coils. In this case, it is possible to reach a frequency match between multiple external fields and result in a beating peak at ultra-low frequencies. Moreover, this peak will be broadened due to various kinds of technique noise, and this situation can seriously disturb the long-term stability of the sensor as discussed in Ref. 7. It is one of the aims of this paper to work out a solution to eliminating this problem.

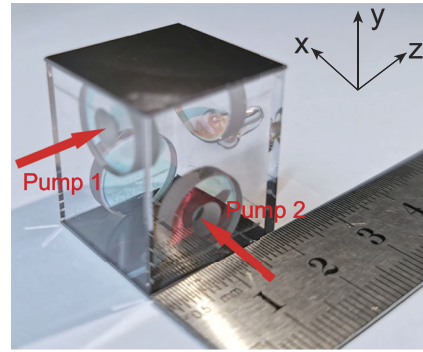


FIG. 1. A picture of the cell used for the magnetometer, and the pump beams injected into each cavity are split from the same beam.

III. ELECTRONICS DESIGN

The whole atomic magnetometer system consists of three parts: the sensor head, the laser, and the signal-processing part, as shown in Fig. 2. The latter two parts are connected with the sensor head through the ports, such as photodiode (PD) detectors and field coils. The signal-processing part needs to realize the closed-loop operation of the sensor so that the bias field along each axis around the cell is nulled constantly. The field programmable gate array (FPGA, Xilinx Virtex-4 XC4VLX40) plays a central role in electronics design. The data acquisition and parameter configurations are implemented by communications between the personal computer (PC) and the FPGA using the universal asynchronous receiver/transmitter (UART) protocol. More details about the laser and the electronics are described in the following subsections.

A. Laser power control

We use a fiber coupled distributed-Bragg-reflector (DBR) laser diode (Photodigm, PH795DBR series) for the sensor. This version of the light source is more compact compared with the free space DBR laser diode (Photodigm, TO-8 package) used in the previous work.⁷ While the power output from the DBR laser diode is stable enough, the power of the beam coupled to the sensor head is subject to disturbances from various sources.

As discussed in Refs. 7, we only need to control the laser power in the sensor head every tens of seconds, so that the power cost of the feedback system can be further reduced. A mechanical fiber attenuator is suitable for this pulsed feedback scheme, where a screw is used to change the attenuating factor. The signal from the power monitor PD is amplified by a transimpedance amplifier (TIA) and then digitized by a 12-bit ADC (ADC128S102). This digital signal is compared with the set point by the FPGA, and the error signal is used to drive a step motor to fine tune the screw of the fiber attenuator every 10 s. In this way, the beam power is constantly kept within 1% inside the sensor head, which is enough for long term field detection stability at the level of pT.

B. Signal processing

The signals for the modulation fields (V_m) are generated by digital signal generators (DSG) of the FPGA, converted to analog

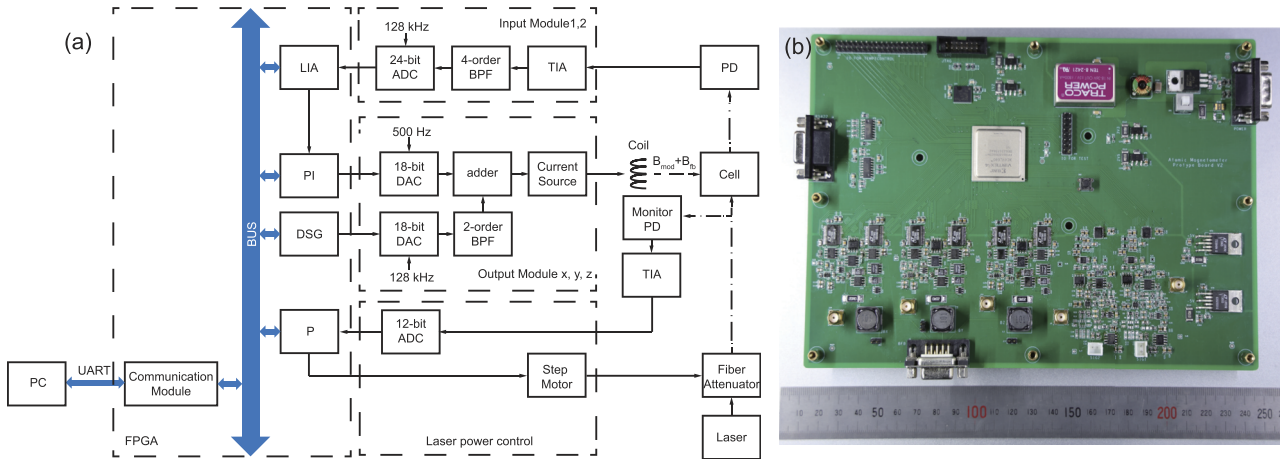


FIG. 2. (a) The design of the atomic magnetometer, including the electronics for signal processing and laser power control. BPF: band-pass filter, DSG: digital signal generator, LIA: lock-in amplifier, P: proportional controller, PD: photodiode detector, PI: proportional–integral controller, and TIA: *trans*-impedance amplifier. (b) A picture of the board for signal-processing electronics.

signals by 18-bit DACs (LTC2756) with an update rate of 128 kHz, and smoothed by a second-order band-pass filter (BPF). The input modules of the signal-processing electronics first convert current signals coming from two photodiodes that detect the transmitted pump beams into voltage signals through TIAs. The information that carries the first harmonics of the modulation fields is kept by passing the signals through 4th-order BPFs. Then, the signals are digitized by 24-bit ADCs (AD7768-1) with an update rate of 128 kHz and are separately demodulated by three lock-in amplifiers (LIA) inside the FPGA for the three sensitive axes of the sensor. These LIA outputs are fed back to PI controllers whose outputs are converted to analog signals by 18-bit DACs (LTC2756) with an update rate of 500 Hz. The feedback signals (V_{fb}) and the modulation signals V_m are added together and sent to control the outputs of Howland current sources,¹⁰ which are connected to the field coils of the sensor.

The field resolution δB_q of the magnetometer at each time of data acquisition can be expressed as

$$\delta B_q = \frac{\delta V_{fb}}{R_{ref}} A_{coil}, \quad (3)$$

where $R_{ref} = 1 \text{ k}\Omega$ is the resistance of the conversion resistor used for controlling the Howland current source output, $A_{coil} \approx 70 \text{ nT/mA}$ is the calibration factor of the field coils inside the sensor head, and δV_{fb} is the quantized resolution of the 18-bit DAC for V_{fb} , which is equal to $(V_{ref+} - V_{ref-})/2^{18}$ with $V_{ref,\pm} = \pm 4.096 \text{ V}$ as the reference voltage of the DAC. The resulting field resolution is $\delta B_q \approx 2 \text{ pT}$ for a single measurement event lasting for 2 ms, which is determined by the update rate $f_s = 500 \text{ Hz}$ of the DAC.

Suppose that the quantization error of the magnetometer is uniformly distributed in the range of $[-\delta B_q/2, \delta B_q/2]$, the resulted average noise power is $\delta B_q^2/12$. The spectral density of this noise is $\sim 26 \text{ fT/Hz}^{1/2}$, which is one of the main contributions to the noise floor of the magnetometer system. This technique noise can be

reduced by increasing R_{ref} in Eq. (3). Here, both the quantization noise from V_m and the thermal noise from the conversion resistor are neglected because the components in the frequency range we focus on have been filtered out for the former one while the magnitude of the latter one is negligible.

C. Some detailed designs inside the FPGA

As mentioned in previous subsections, the control FPGA implements the operations of DSGs, LIAs, and PI controllers, as shown in Fig. 3. In this subsection, we add more details on these operations.

Each modulation field and the reference signal of each LIA are generated by DSG modules. A DSG module consists of a phase module and a function generator (FG) module. The phase module generates the phase output using an accumulator (AX). The FG module generates a sinusoidal signal using the coordinate-rotation-digital-computer (CORDIC) algorithm.¹¹

For each LIA, the multiplication result of the input signal and the reference signal is sent to a low-pass filter (LPF). In this work, to reduce the cost of resources while maintaining the performance, we use the cascaded-integrator-comb (CIC) LPFs.¹² A CIC LPF is effectively a recursive running average of a sample with a comb separation of D , and its implementation only involves basic operations of summing and shifting when D is integer powers of 2. The transfer function of an n th-order CIC LPF in the z -domain is

$$H(z) = \left(\frac{1}{D} \frac{1 - z^{-D}}{1 - z^{-1}} \right)^n. \quad (4)$$

In our case, we use a fifth-order ($n = 5$) CIC LPF with a sampling rate of $f_s = 16 \text{ kHz}$ and a comb separation of $D = 32$. The magnitude response of this LPF is shown in Fig. 4, where the zero-response points appear at integer harmonics of f_s/D .

Due to various reasons, there is a phase shift between the driving field and the response from the sensor head. This phase shift is

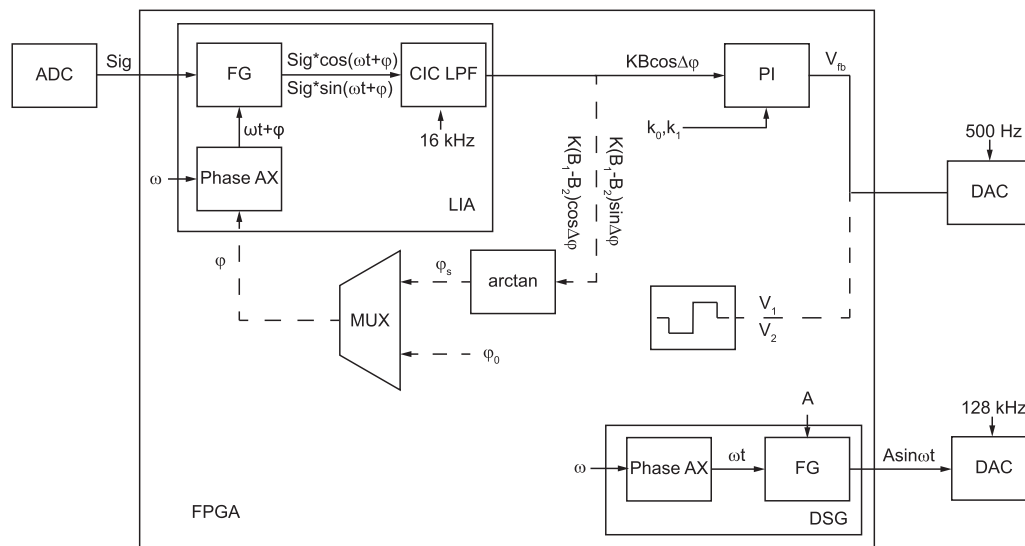


FIG. 3. Some key operations inside the control FPGA. The dashed lines denote the signal processes to determine the optimized phase of the LIA while the sensor operates in the open loop mode. The input of A and ω for DSG is the amplitude and frequency of the generated sinusoidal signals. AX: accumulator, FG: function generator, LFP: low-pass filter, and MUX: multiplexer.

mainly dependent on the cell temperature and the frequency of the driving field. Therefore, we treat this phase shift as a constant once the cell temperature and driving field parameters are fixed. Such a shift for the measurement result of each axis is calibrated by sending two bias fields B_1 and B_2 to the field coils along this axis while the sensor is running in the open loop mode. The phase shift is extracted using the in-phase and out-of-phase outputs of LIA (see Fig. 3). We then use a multiplexer (MUX) to select the correct offset phase calculated from the measurement result for the phase AX to compensate for the aforementioned phase shift. This operation is automatically performed after the startup of FPGA to assure that the sensor works with the best sensitivity in the following measurements. Then the feedback loop is closed, where digital position-form PI controllers

are used. Suppose that a set of data (e) is sent to such a PI controller with a set-point at zero and k_p (k_i) is the coefficient of the proportional (integral) part, the output data u from this controller is

$$u(m) = k_p e(m) + k_i \sum_{k=0}^m e(k) = u(m-1) + k_0 e(m) - k_1 e(m-1), \quad (5)$$

where $k_0 = k_p + k_i$ and $k_1 = k_p$. The digital PI outputs are recorded by the PC as the magnetometer measurement results.

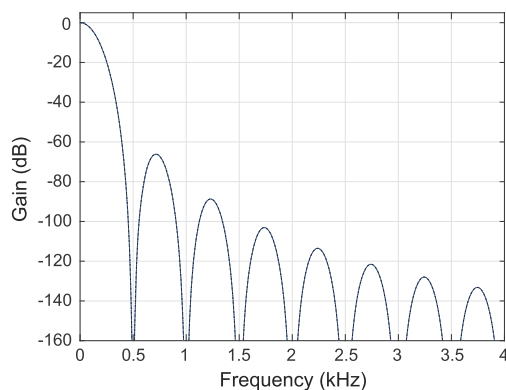


FIG. 4. Magnitude response of a 5th-order CIC LFP with a sampling rate of 16 kHz and a comb separation of $D = 32$.

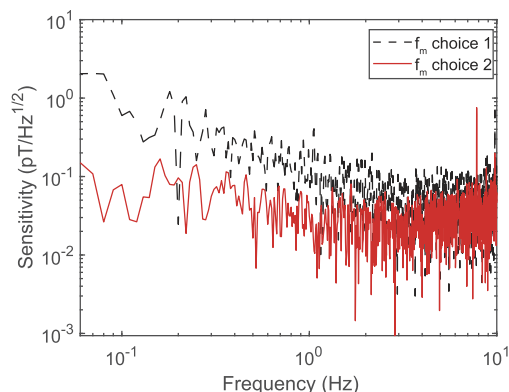


FIG. 5. Comparisons of the sensor sensitivity in the x axis for two choices of modulation frequencies (f_m). The frequency choice 1 corresponds to $f_1 = 1.875$ kHz, $f_2 = 2.375$ kHz, and $f_3 = 2.875$ kHz. Choice 2 corresponds to $f_1 = 1.57$ kHz, $f_2 = 2.07$ kHz, and $f_3 = 3.07$ kHz.

IV. EXPERIMENT RESULTS

As shown in Fig. 4, the zero-magnitude response points of the CIC LPF used in this work distribute at harmonics of 500 Hz. We make use of this property by choosing the modulation field frequencies (f_1 , f_2 , and f_3 in the ascending order) so that their separations match the zero-response frequencies of the CIC LPF. In this way, we can eliminate the maximum amount of the beating signals between the first harmonics of the modulation frequencies in the LIA output. Otherwise, some parts of these beating signals would survive the LPF, enter the field coils as real fields, and generate low frequency noise from further interferences as explained in Sec. II.

This frequency-selection scheme turns out to be a simple and robust method to suppress the signal-interference problem. However, special care is needed to avoid the case $f_2 - f_1 = f_3 - f_2$. In this case, although the CIC LPF eliminates the beating signal from two of the modulation fields in the feedback loop, a higher order beating peak appears at zero Hz, which can not be eliminated by the CIC LPF. Similar to the discussions in Sec. II, this zero peak will be broadened due to technique noise, and it leads to a higher level of noise at low frequency domain. This is confirmed by the experimental results in Fig. 5, which compares the sensor sensitivity in two cases, one with $f_2 - f_1 = f_3 - f_2$ and the other one with $f_2 - f_1 = (f_3 - f_2)/2$.

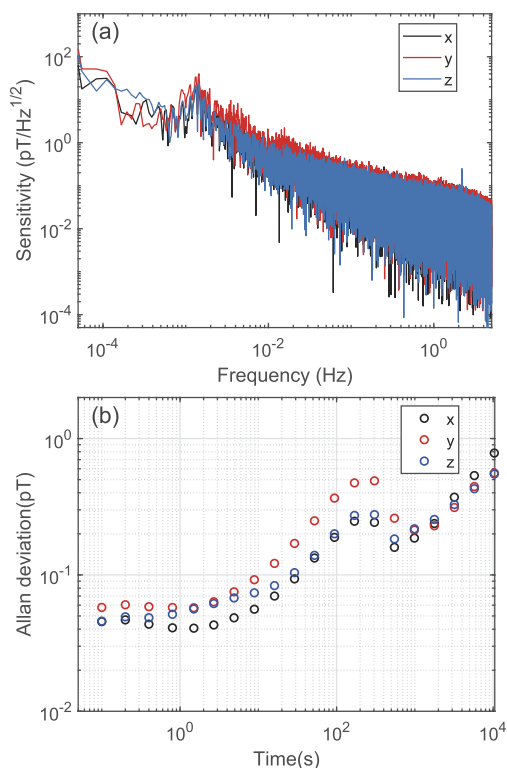


FIG. 6. Plot (a) is the sensor sensitivity plot for a 10-h-long magnetometer data. Plot (b) is the Allan deviation results of the measurement results in plot (a).

The frequencies of the modulation fields for the sensor are set at $f_1 = 1.57$ kHz, $f_2 = 2.07$ kHz, and $f_3 = 3.07$ kHz. With a cell temperature of 75 °C, electronics parameters set to limit the sensor bandwidth as 30 Hz, and the aforementioned pulsed laser-power controller on, we record measurement results of the sensor for 10 hours using the signal-processing electronics developed in this work. The frequency-domain and time-domain analyses of the recorded data are shown in Figs. 6(a) and 6(b), respectively. The field sensitivity is better than 40 fT/Hz^{1/2} at 1 Hz for all three axes, and the bump around 1 mHz is caused by the instability of the cell temperature, which is controlled based on a T-type thermal couple. The drift of the measurement results is less than 1 pT with an integration time of 10⁴ s for each axis. These sensor performances are on the same level as, if not better than, the results in Ref. 7.

V. OUTLOOK

The ultimate miniaturization of the magnetometer system requires the development of home-made compact and precision electronics for laser control, which mainly include the control of the temperature and current of the laser diode. We have finished the preliminary designs of both controllers and separately tested their performance. We will integrate these laser control electronics with the FPGA-based signal-processing electronics in the following work.

ACKNOWLEDGMENTS

This work was partially carried out at the University of Science and Technology of China (USTC) Center for Micro and Nanoscale Research and Fabrication. This work was supported by the National Natural Science Foundation of China (NSFC, Grant No. 11974329) and the Scientific Instrument and Equipment Development Projects, Chinese Academy of Sciences (CAS, Grant No. YJKYYQ20200043).

AUTHOR DECLARATIONS

Conflict of Interest

The authors have no conflicts to disclose.

Author Contributions

H. Zhou: Methodology (lead); Software (lead); Validation (lead); Writing – original draft (lead). **X.-K. Wang:** Methodology (supporting); Software (supporting); Validation (supporting). **S.-Q. Liu:** Methodology (supporting); Validation (supporting). **L. Cheng:** Methodology (supporting); Validation (supporting). **K. Liu:** Funding acquisition (supporting); Project administration (equal). **Z.-H. Pan:** Funding acquisition (supporting); Project administration (equal). **Y.-R. Li:** Funding acquisition (supporting); Project administration (equal). **X.-J. Hao:** Conceptualization (equal); Funding acquisition (equal); Investigation (equal); Supervision (equal); Writing – review & editing (equal). **D. Sheng:** Conceptualization (equal); Funding acquisition (equal); Investigation (equal); Supervision (equal); Writing – review & editing (equal). **Y.-M. Wang:** Funding acquisition (lead); Project administration (lead).

DATA AVAILABILITY

The data that support the findings of this study are available from the corresponding author upon reasonable request.

REFERENCES

- ¹M. S. Safronova, D. Budker, D. DeMille, D. F. J. Kimball, A. Derevianko, and C. W. Clark, "Search for new physics with atoms and molecules," *Rev. Mod. Phys.* **90**, 025008 (2018).
- ²S. Afach, B. C. Buchler, D. Budker, C. Dailey, A. Derevianko, V. Dumont, N. L. Figueroa, I. Gerhardt, Z. D. Grujić, H. Guo, C. Hao, P. S. Hamilton, M. Hedges, D. F. Jackson Kimball, D. Kim, S. Khamis, T. Kornack, V. Lebedev, Z.-T. Lu, H. Masia-Roig, M. Monroy, M. Padniuk, C. A. Palm, S. Y. Park, K. V. Paul, A. Penaflor, X. Peng, M. Pospelov, R. Preston, S. Pustelny, T. Scholtes, P. C. Segura, Y. K. Semertzidis, D. Sheng, Y. C. Shin, J. A. Smiga, J. E. Stalnaker, I. Sulai, D. Tandon, T. Wang, A. Weis, A. Wickenbrock, T. Wilson, T. Wu, D. Wurm, W. Xiao, Y. Yang, D. Yu, J. Zhang, and GNOME Collaboration, "Search for topological defect dark matter with a global network of optical magnetometers," *Nat. Phys.* **17**, 1396–1401 (2021).
- ³O. Alem, R. Mhaskar, R. Jiménez-Martínez, D. Sheng, J. LeBlanc, L. Trahms, T. Sander, J. Kitching, and S. Knappe, "Magnetic field imaging with microfabricated optically-pumped magnetometers," *Opt. Express* **25**, 7849–7858 (2017).
- ⁴E. J. Pratt, M. Ledbetter, R. Jiménez-Martínez, B. Shapiro, A. Solon, G. Z. Iwata, S. Garber, J. Gormley, D. Decker, D. Delgadillo, A. T. Dellis, J. Phillips, G. Sundar, J. Leung, J. Coyne, M. McKinley, G. Lopez, S. Homan, L. Marsh, M. Zhang, V. Maurice, B. Siepser, T. Giovannoli, B. Leverett, G. Lerner, S. Seidman, V. DeLuna, K. Wright-Freeman, J. Kates-Harbeck, T. Lasser, H. Mohseni, T. Sharp, A. Zorzos, A. H. Lara, A. Kouhzadi, A. Ojeda, P. Chopra, Z. Bednarke, M. Henninger, and J. K. Alford, "Kernel flux: A whole-head 432-magnetometer optically-pumped magnetoencephalography (OP-MEG) system for brain activity imaging during natural human experiences," in *Optical and Quantum Sensing and Precision Metrology*, edited by S. M. Shahriar and J. Scheuer (International Society for Optics and Photonics, SPIE, 2021), p. 1170032, Vol. 11700.
- ⁵M. D. Prouty, R. Johnson, I. Hrvoic, and A. K. Vershovskiy, "Optical magnetometry: Geophysical applications," in *Optical Magnetometry* (Cambridge University Press, 2013), pp. 319–333.
- ⁶M. H. Acuña, "Space-based magnetometers," *Rev. Sci. Instrum.* **73**, 3717–3736 (2002).
- ⁷S. Liu, Q. Yu, H. Zhou, and D. Sheng, "Sensitive and stable atomic vector magnetometer to detect weak fields using two orthogonal multipass cavities," *Phys. Rev. Applied* **19**, 044062 (2023).
- ⁸C. Abel, S. Afach, N. J. Ayres, G. Ban, G. Bison, K. Bodek, V. Bondar, E. Chanel, P.-J. Chiu, C. B. Crawford, Z. Chowdhuri, M. Daum, S. Emmenegger, L. Ferraris-Bouchez, M. Fertl, B. Franke, W. C. Griffith, Z. D. Grujić, L. Hayen, V. Hélaine, N. Hild, M. Kasprzak, Y. Kermaidic, K. Kirch, P. Knowles, H.-C. Koch, S. Komposch, P. A. Koss, A. Kozela, J. Krempel, B. Lauss, T. Lefort, Y. Lemièrre, A. Leredde, A. Mtchedlishvili, P. Mohanmurthy, M. Musgrave, O. Naviliat-Cuncic, D. Pais, A. Pazgalev, F. M. Piegsa, E. Pierre, G. Pignol, P. N. Prashanth, G. Quémener, M. Rawlik, D. Rebreyend, D. Ries, S. Roccia, D. Rozpedzik, P. Schmidt-Wellenburg, A. Schnabel, N. Severijns, R. T. Dinani, J. Thorne, A. Weis, E. Wursten, G. Wyszynski, J. Zejma, and G. Zsigmond, "Optically pumped Cs magnetometers enabling a high-sensitivity search for the neutron electric dipole moment," *Phys. Rev. A* **101**, 053419 (2020).
- ⁹S. Appelt, A. B.-A. Baranga, C. J. Erickson, M. V. Romalis, A. R. Young, and W. Happer, "Theory of spin-exchange optical pumping of ^3He and ^{129}Xe ," *Phys. Rev. A* **58**, 1412–1439 (1998).
- ¹⁰P. Horowitz and W. Hill, *The Art of Electronics*, 3rd ed. (Cambridge University Press, 2015).
- ¹¹J. E. Volder, "The CORDIC trigonometric computing technique," *IRE Trans. Electron. Comput.* **EC-8**, 330–334 (1959).
- ¹²E. Hogenauer, "An economical class of digital filters for decimation and interpolation," *IEEE Trans. Acoust., Speech, Signal Process.* **29**, 155–162 (1981).